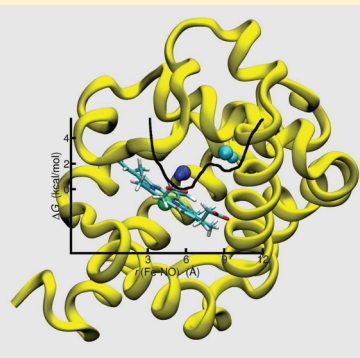


Molecular Dynamics Simulation of Nitric Oxide in Myoglobin

Myung Won Lee and Markus Meuwly*

Department of Chemistry, University of Basel, Klingelbergstrasse 80, 4056 Basel, Switzerland

ABSTRACT: The infrared (IR) spectroscopy and ligand migration of photodissociated nitric oxide (NO) in and around the active sites in myoglobin (Mb) are investigated. A distributed multipolar model for open-shell systems is developed and used, which allows one to realistically describe the charge distribution around the diatomic probe molecule. The IR spectra were computed from the trajectories for two conformational substates at various temperatures. The lines are narrow (width of 3–7 cm⁻¹ at 20–100 K), in agreement with the experimental observations where they have widths of 4–5 cm⁻¹ at 4 K. It is found that within one conformational substate (B or C) the splitting of the spectrum can be correctly described compared with recent experiments. Similar to photodissociated CO in Mb, additional substates exist for NO in Mb, which are separated by barriers below 1 kcal/mol. Contrary to full quantum mechanical calculations, however, the force field and mixed QM/MM simulations do not correctly describe the relative shifts between the B- and C-states relative to gas-phase NO. Free energy simulations establish that NO preferably localizes in the distal site and the barrier for migration to the neighboring Xe4 pocket is $\Delta G_{B \rightarrow C}^{\ddagger} = 1.7\text{--}2.0$ kcal/mol. The reverse barrier is $\Delta G_{C \rightarrow B}^{\ddagger} = 0.7$ kcal/mol, which agrees well with the experimental value of 0.7 kcal/mol, estimated from kinetic data.



I. INTRODUCTION

Nitric oxide (NO) is a key messenger involved in many biological processes in vertebrates. It can bind to myoglobin (Mb) and together with O₂ can be catalyzed by Mb to form nitrate.¹ As with carbon monoxide (CO), NO is a versatile and useful local probe for the electrostatic environment of a protein. For example, a linear correlation between the stretching frequencies of heme-bound NO and CO has been found by screening a large array of ferrous MbNO samples.² On the other hand, the rebinding kinetics of NO to Mb differs from that of CO. This process has been studied intensively over the past two decades using experimental and computational methods.^{3–15} Compared to rebinding of CO, no substantial rebinding barrier has been found for geminate recombination of NO to the heme-iron,⁴ and ab initio calculations have even suggested that the recombination reaction may be barrierless for NO in specific conformations.¹⁶ Because of the short time scale involved, this process is ideally suited to be investigated computationally at an atomistic level.^{11–15} As the difference in the kinetics depends on the details of the electronic structures of NO and CO, it would be highly desirable to have force fields that can accurately describe the electrostatics around diatomic molecules such as CO and NO.

A ligand molecule in the empty space just above the heme-iron atom in Mb, called the heme pocket or distal cavity (spectroscopic B-state), can interact with the iron atom directly. In addition, there are four prominent cavities in Mb (Xe1 through Xe4) which were discovered from X-ray crystallography of Xe-pressurized Mb.¹⁷ Among the four Xe cavities, the Xe4 cavity (spectroscopic C-state) is closest to the heme pocket and a ligand can move readily between the heme pocket and the Xe4 cavity. This has been explicitly found for CO in a Mb

mutant from time-resolved X-ray crystallography.¹⁸ As the passage of a ligand between the B- and C-state may be an important step in reactions catalyzed by Mb, we study the migration of the ligand between these two sites in addition to the possible substates in both cavities in the present work.

Mb is a single-chain globular protein containing a heme group and is found in the muscle tissue of vertebrates in general. While Mb has been known primarily as a dioxygen storage protein, Mb also has the capability to catalyze reactions among small molecules (NO, CO, and O₂) by concentrating and orienting them.¹ It has been suggested from kinetic experiments of CO in Mb that several states exist in equilibrium for ligands within Mb¹⁹



where A is the ligand-bound state, S is the state with the ligand in the solvent, and B, C, and D are states in between. Experimental studies²⁰ have provided information on the physical location of the CO ligand for various states described above: CO in the heme pocket is associated with the spectroscopic B-state and CO in the Xe4 cavity with the C-state.¹⁸ This is also the nomenclature followed in the present work, which associates the B-state with the NO ligand in the heme pocket (not bound to Fe) and the C-state with the ligand in the Xe4 cavity.

While electrostatic interactions in conventional force fields are commonly described by individual point charges on atoms, the accuracy of such a model can be improved by including

Received: December 15, 2011

Revised: March 14, 2012

Published: March 15, 2012

higher multipole moments (MTPs). The use of higher MTPs for CO has been validated extensively for Mb–CO,^{21–23} and it has been shown that an accurate description of CO is essential for correctly reproducing the infrared (IR) spectra. Even though two point charges for a diatomic molecule can reproduce its overall charge and dipole moment, it is not possible to correctly describe its quadrupole moment. Because electrostatic models based on fluctuating^{14,22,24–26} and multipolar²¹ charge distributions have provided important insights into the energetics, dynamics, and spectroscopy of small ligands in protein and condensed-phase environments,^{27,28} an extension of multipole-based models to open-shell ligands such as nitric oxide is presented here. The quantitative analysis of spectroscopic and energetic properties of NO in Mb is also warranted by more recent experiments which investigated the IR spectra of NO in different conformational substates²⁹ and ligand migration between them.⁷ In particular, a recent rebinding study left points unanswered concerning questions as to the identity of site "X" from which the photodissociated ligand rebinds to the heme-iron.⁷

Compared to CO, the inclusion of MTPs may be more important in the case of NO because the unpaired electron breaks the cylindrical symmetry of the molecule around the molecular axis. It is possible to reproduce the reduced symmetry if we include MTP terms on the N and O atoms that generate asymmetric electrical fields, whereas the inclusion of MTP terms in the case of CO leads to cylindrical symmetry. In the present work, we extend the use of atom-centered MTPs to open-shell systems and use it to characterize and discuss opportunities and limitations to investigate structural, energetic, and spectroscopic properties of photolyzed NO in Mb and furthermore a spectroscopic probe in proteins in general.

II. COMPUTATIONAL METHODS

All molecular dynamics (MD) simulations were carried out using the CHARMM program³⁰ with provisions for calculating multipolar interactions.²¹ The initial structure of MbNO is 1HJT³¹ from the Protein Data Bank (PDB),³² which is the structure of the ferrous nitric oxide form of native sperm whale Mb determined by X-ray crystallography at 1.7 Å resolution. First, hydrogen atoms were added to the protein, for which the ε tautomer was chosen for the His64 residue.^{33–35} Next, the protein including the ligand was solvated in a cubic water box of side length 58 Å, containing ~17 500 water molecules. After solvation, the protein structure was optimized and the system was heated to 300 K for 20 ps and further equilibrated for 25–120 ps at 300 K. Then, production simulations in the NPT ensemble followed. For the water molecules, the TIP3P model³⁶ was used together with SHAKE.^{37,38} Typically, 20 independent simulations, each 2 ns in length, were run and the time step was $\Delta t = 1$ fs. The structure of the simulation system is shown in Figure 1, with the NO molecule in the heme pocket (spectroscopic B-state) or Xe4 cavity (C-state) at 20 K, and water molecules are not displayed for clarity.

Most simulations were carried out with periodic boundary conditions (PBC). The nonbonded interactions (electrostatic and van der Waals) were truncated at a distance of 12 Å and switched between 10 and 12 Å. To establish the effect of very long electrostatic cutoffs on the IR spectra, multiple independent 1 ns NVT simulations were carried out without electrostatic cutoff and using spherical boundary conditions (SBC),³⁹ with Mb surrounded by a water sphere of radius 19 Å centered around the Fe atom of the heme group.

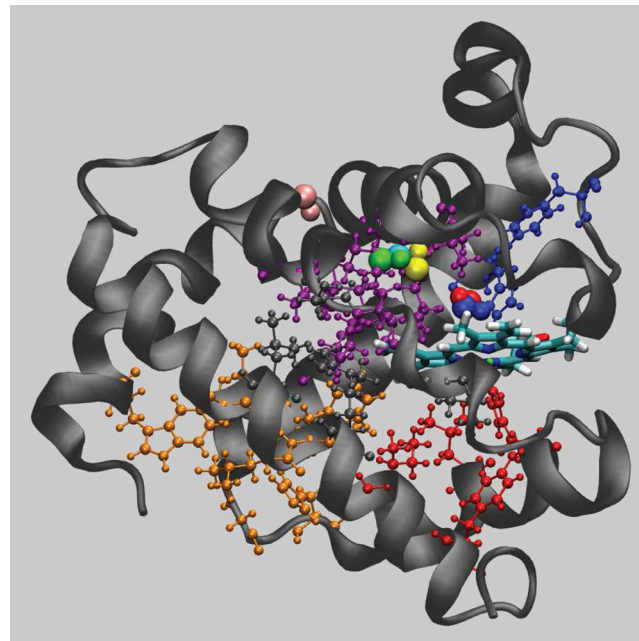


Figure 1. The structure of MbNO with the NO molecule in the heme pocket (red or blue spheres) or in the Xe4 cavity (green, cyan, or yellow). The N atom of NO is the larger sphere, and both N and O atoms are displayed in the same color for the same state. The structure was obtained at 20 K with NO in various states. NO in the heme pocket with $\angle(\text{Fe}-\text{N}-\text{O}) \approx 60^\circ$ (blue) and 110° (red) and in the Xe4 cavity with $\angle(\text{Fe}-\text{N}-\text{O}) \approx 60^\circ$ (green), 110° (cyan), and 150° (yellow). The position of NO outside the heme pocket and the Xe4 cavity is shown in pink spheres, obtained from a trajectory at 300 K with NO initially in the Xe4 cavity. The residues lining the heme pocket or Xe cavities are displayed with the ball-and-stick model: heme pocket (blue), Xe4 (purple), Xe1 (red), Xe2 (gray), and Xe4 (orange).

The stretching potential of the nitric oxide molecule was described by a Morse potential

$$V(r) = D_e \{1 - \exp[-\beta(r - r_e)]\}^2 \quad (2)$$

where $D_e = 152.6$ kcal/mol, $\beta = 2.636$ Å, and $r_e = 1.151$ Å were taken from previous work.²⁴ The Lennard-Jones (LJ) parameters for the N and O atoms of the NO molecule were $\epsilon^N = 0.20$ kcal/mol, $\epsilon^O = 0.16$ kcal/mol, $r_{\min}^N/2 = 2.00$ Å, and $r_{\min}^O/2 = 2.05$ Å.¹³ This parametrization yields a fundamental anharmonic gas-phase frequency of 1833 cm^{-1} . Experimentally, free NO absorbs at 1876 cm^{-1} .^{40,41} In comparing IR spectra computed from the Fourier transform of the dipole autocorrelation function (see below) with experimental frequencies, it has to be remembered that a constant offset of $\sim 40\text{ cm}^{-1}$ arises due to two effects. First, it has been noted from simulations of CO in argon⁴² that the integration of the equations of motions using the velocity-Verlet algorithm with a time step of 1 fs shifts the frequency by 16 cm^{-1} . The remaining difference (27 cm^{-1}) can be attributed to the classical treatment of the anharmonic oscillator, which has an energy-dependent fundamental frequency.²¹ These corrections affect all spectroscopic features equally and therefore do not influence relative positions of spectral lines. In the following, all frequencies are reported relative to $\nu_0 = 1833\text{ cm}^{-1}$.

The NO multipole moments were calculated at bond distances between 0.95 and $1.05r_e$ from 11 unrestricted DFT/B3LYP calculations with the aug-cc-pVQZ basis set using Gaussian 03 (G03).⁴³ Then, the charges, dipole

Table 1. Multipole Moments of NO Computed from DFT/B3LYP with aug-cc-pVQZ^a

	$Q_{00}^o (e)$	$Q'_{00} (ea_0^{-1})$	$Q_{10}^o (ea_0)$	$Q'_{10} (e)$	$Q_{20}^o (ea_0^2)$	$Q'_{20} (ea_0)$	$Q_{22c}^o (ea_0^2)$	$Q'_{22c} (ea_0)$
N	0.065	0.195	0.514	-0.600	0.379	-0.275	0.505	-0.254
O	-0.065	-0.195	-0.323	0.519	0.572	-0.070	0.228	-0.060

^aEach multipole component is described by $Q_u = Q_u^o + Q'_u(r - r_e)$, where u represents angular momentum labels (00, 10, 11c, 11s, 20, 21c, 21s, 22c, and 22s). The unit of r is bohr (a_0), and the units of Q_u^o and Q'_u are given in parentheses in the table. Only nonzero components are shown.

moments, and quadrupole moments on the N and O atoms were calculated with the GDMA program⁴⁴ by

$$Q_{lk} = \int R_{lk}(\mathbf{r})\rho(\mathbf{r}) d^3\mathbf{r} \quad (3)$$

Here, Q_{lk} is the spherical harmonic multipole, $R_{lk}(\mathbf{r})$ the regular solid harmonics, and $\rho(\mathbf{r})$ the total charge density. Each component (charge, dipole moment, and quadrupole moment) was fit to a linear dependence with respect to the bond distance, and the slope and y -intercept were obtained with a correlation coefficient of $R^2 \approx 1.0$. The values of all nonzero components up to quadrupole moments are summarized in Table 1. The computed molecular dipole and quadrupole moments of NO are $0.050 ea_0$ and $1.14 ea_0^2$, and agree well with the experimental values of $0.060 \pm 0.004 ea_0^{45}$ and $1.01 ea_0^2$.⁴⁶

For closed-shell diatomic molecules, such as carbon monoxide (CO), the only nonzero quadrupole component is Q_{20} . In this case, it is sufficient to define a local z -axis which is parallel to the bond. Contrary to that, NO has an additional nonzero component Q_{22c} due to its unpaired electron, as shown in Table 1. For this reason, it is necessary to introduce additional local (molecule-fixed) x - and y -axes in order to calculate the energies and forces due to the quadrupole moments.^{44,47,48} For example, the interaction between a point charge and Q_{20} is given by $(3r_z^2 - 1)/2R^3$, while that between a point charge and Q_{22c} by $3^{1/2}(r_x^2 - r_y^2)/2R^3$, where $r_\alpha = \mathbf{e}_\alpha \cdot \mathbf{u}$ with $\alpha = x, y$, or z , and R is the distance between the point charge and the quadrupole moment (Q_{20} or Q_{22c}).⁴⁷ \mathbf{e}_α denotes the unit vectors of the local axis system for the quadrupole moment and \mathbf{u} the unit vector connecting the quadrupole moment and the point charge. For a cylindrically symmetric charge distribution, such as for CO, only one axis—usually the z -axis—is required, whereas a more comprehensive axis system is needed if there is any nonzero term other than Q_{20} , such as Q_{22c} , as in the case of NO. For this, the implementation in CHARMM (c36a1) was suitably modified. Technically, a dummy atom X (without charge or higher electrical moments) bonded to the nitrogen atom of NO was introduced. The position of X was defined by the X–N bond length $r_{XN} = 1.5 \text{ \AA}$ and the XNO angle $\theta_{XNO} = 120^\circ$, as illustrated in Figure 2. The specific values of r_{XN} and θ_{XNO} were found to not affect the results from the simulations. The position of the dummy atom is necessary to define the local x - and y -axes. While the values of r_{XN} and θ_{XNO} have no physical meaning, the direction of the dummy atom relative to the NO molecule corresponds to the direction of the molecular orbital for the unpaired electron of

NO. As electrons move much faster than the nuclei, it is appropriate to assume that they rearrange instantaneously. Consequently, the orientation of the unpaired electron is given by the configuration that minimizes the energy of the NO molecule relative to its environment. To this end, the dihedral angle of $X^{\text{new}}-\text{N}-\text{O}-X^{\text{old}}$ was scanned for X^{new} at each MD step to determine the new position of X that minimizes the total energy. Due to the symmetry of the molecule, it is sufficient to scan the torsional angle from 0 to 180° . In the present work, the torsional angle was scanned in 5° intervals. As previous work indicated that the dynamics of small probes can be sensitive to the van der Waals ranges r_{\min} , additional simulations with r_{\min} of the N and O atoms modified by $\pm 10\%$ were carried out.⁴⁹

The IR spectrum along a particular trajectory is calculated from the Fourier transform of the NO-dipole moment autocorrelation function $C(t)$ accumulated over 2^n time origins, where n is an integer such that 2^n corresponds to between 1/3 and 1/2 of the trajectory, with the time origins separated by 1 fs. $\hat{C}(\omega)$, which is the Fourier transform of $C(t)$, is computed using a fast Fourier transform (FFT) with a Blackman filter to reduce noise.⁵⁰ The final IR absorption spectrum $A(\omega)$ is then calculated from

$$A(\omega) \propto \omega \{1 - \exp[-\hbar\omega/(k_B T)]\} \hat{C}(\omega) \quad (4)$$

where k_B is the Boltzmann constant and T is the absolute temperature in kelvin.

IR spectra in the condensed phase can also be computed from the forces arising from the electrical field and acting along the bond of the vibrating molecule. Such an approach, which separates the molecular dynamics from the calculation of the spectroscopic response, has been pursued for CO in Mb.^{51,52} These studies were, however, not successful in explaining important experimental observations such as the splitting of the spectral line in going from the gas to the condensed phase. On the other hand, a so-called map-based approach has been applied successfully in the simulations of IR spectra of liquid water, where—probably due to substantial averaging over a large number of molecules—important features of the spectroscopy could be captured.^{53,54} Again, nuclear dynamics and computation of spectral features are separated in such an approach because conformational sampling is carried out with a (usually rigid) water model, whereas the spectroscopy along the O–H bonds is computed from a highly accurate map.

Free energy barriers for NO migration between the heme pocket and the Xe4 cavity were determined from umbrella sampling simulations.⁵⁵ The umbrella potential has the form

$$U(\delta) = K(\delta - \delta_0)^2 \quad (5)$$

where K is the strength of the biasing potential and δ_0 the center of the umbrella window. The reaction coordinate δ is the distance between the center of mass of NO and the iron atom of the heme group, which has been shown to be meaningful in previous simulations of MbCO and MbNO.²⁴ A total of 12

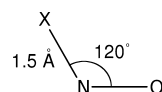


Figure 2. The structure of the NO molecule with the dummy atom X, as used in the simulations. X is bonded to the N atom at a distance $r_{XN} = 1.5 \text{ \AA}$ and at an angle $\theta_{XNO} = 120^\circ$.

Table 2. Energies of NO–H₂O Complex (I) from CHARMM at CHARMM-Minimized Structures, (II) from DFT/B3LYP at CHARMM-Minimized Structures, and (III) from DFT/B3LYP at DFT/B3LYP-Optimized Structures

	(I)		(II)		(III)	
	E (kcal/mol)	ΔE (kcal/mol)	E (hartree)	ΔE (kcal/mol)	E (hartree)	ΔE (kcal/mol)
1	-153.476	0.284	-206.23752	0.262	-206.23777	0.331
2	-152.908	0.852	-206.23727	0.417	-206.23754	0.478
3	-153.760	0.000	-206.23793	0.000	-206.23830	0.000
4	-153.284	0.476	-206.23729	0.401	-206.23769	0.384

windows with values of δ_0 between $1 \text{ \AA} \leq \delta_0 \leq 12 \text{ \AA}$ were used with $K = 5.0 \text{ kcal}\cdot\text{mol}^{-1}\cdot\text{\AA}^{-2}$. The simulations were carried out at 300 K with an equilibration time of 210 ps for every window, after which data accumulation was carried out for 100 ps per window. The free energy change along the NO migration path is the potential of mean force $W(\delta)$ which is defined as

$$W(\delta) = -k_B T \ln[P(\delta)] - U(\delta) + C_i \quad (6)$$

where $P(\delta)$ is the equilibrium distribution in the presence of the biasing potential and C_i is a different constant for each window. The weighted histogram analysis method (WHAM) program^{56,57} was used to determine C_i values. For comparison, we also adjusted C_i values without using WHAM by matching the overlap regions between consecutive umbrella windows.⁵⁸

III. RESULTS AND DISCUSSION

In order to validate the computational strategy, the energies of a water–NO complex at four different configurations were compared after minimization with the water molecule treated as a TIP3P water. The DFT/B3LYP energies at CHARMM-minimized structures and DFT/B3LYP-optimized structures were also computed for comparison using the 6-31++G** basis set. They agree well, as shown in Table 2. We also analyzed the electron localization function (ELF)⁵⁹ of the water–NO complex, which shows that the HOMO is occupied by the unpaired electron.

NO Dynamics in the Distal Site and the Xe4 Pocket.

First, the conformational dynamics of NO in and around the heme pocket and the Xe4 cavity was considered. In Figure 1, the NO molecule in the heme pocket (B-state) is displayed as blue or red spheres, and NO in the Xe4 cavity (C-state) as green, cyan, or yellow spheres. The distance between the center of the cavity (B- or C-state, respectively) and the NO molecule during a typical production run is shown in Figure 3 for two different initial conditions: with NO initially in the B- and C-states, respectively. If NO is initially in the heme cavity, the ligand ended up in the same site after 2 ns in 75% of the cases (15 out of 20 trajectories). Detailed analysis revealed that the NO molecule remained in the B-state for the entire 2 ns only for some trajectories, whereas in the majority of cases the unbound ligand moved back and forth between the B- and C-state before finally returning to the heme cavity. In the remaining cases, NO moved into the Xe4 (three trajectories) or Xe1 cavity (two trajectories).

Conversely, with NO initially in the C-state, only in 2 out of 20 trajectories was the ligand found to remain there after 2 ns, whereas migration to the heme pocket was found for 15 trajectories and to another site for 3 trajectories. This site corresponds to the Ph1 cavity found from the extended MD simulations of MbCO.^{60,61} The NO molecule in this site is shown in pink spheres in Figure 1. The spontaneous return of the NO to the B-state for trajectories initiated from the C-state suggests that NO is stabilized in state B relative to C. However,

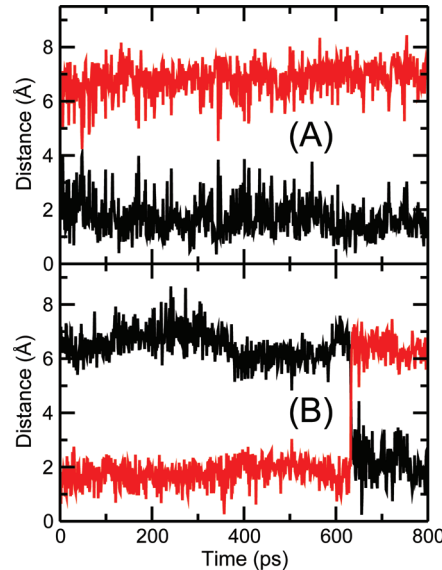


Figure 3. The distance between NO and the center of the heme pocket (black curve) and the Xe4 cavity (red curve). (A) Trajectory started from the B-state and (B) trajectory started from the C-state. After 600 ps, a transition from C to B is observed. More frequent C → B transitions are observed compared with B → C transitions, when many trajectories are monitored.

for a more quantitative assessment, free energy simulations are necessary which are discussed further below.

IR Spectra in the Different Pockets. The IR spectrum is a sensitive probe of the local electric field surrounding the probe molecule, NO in this case. The averaged IR spectra from 20 independent simulations, 1 ns each, at 300 K show a peak intensity at 1840 cm^{-1} for the B-state and at 1839 cm^{-1} when NO started in the C-state, respectively (see Figure 4A). This compares with 1833 cm^{-1} from simulations of free NO in the gas phase and corresponds to a blue shift of $6\text{--}7 \text{ cm}^{-1}$. Experimentally, free NO absorbs at 1876 cm^{-1} ,^{40,41} whereas, in the protein, the NO absorptions shift to $1852\text{--}1869 \text{ cm}^{-1}$, depending on the conformational substate.²⁹ This amounts to red shifts between 7 and 24 cm^{-1} .

As the NO molecule can move between the cavities, the IR spectra shown in Figure 4A as dashed lines contain contributions from all cavities the ligand visits during the MD simulation. To obtain pocket-specific spectra at 300 K, we selected parts of the trajectories where the NO molecule remains only in one cavity and then computed the corresponding IR spectra which are shown in Figure 4A as solid lines. The intensity on the red side of the main peak is somewhat higher for the B-state (black solid line) compared to that for the C-state (red solid line). It is noteworthy that the IR spectrum computed from the entire trajectories started from the C-state (red dashed line) also shows an increased intensity

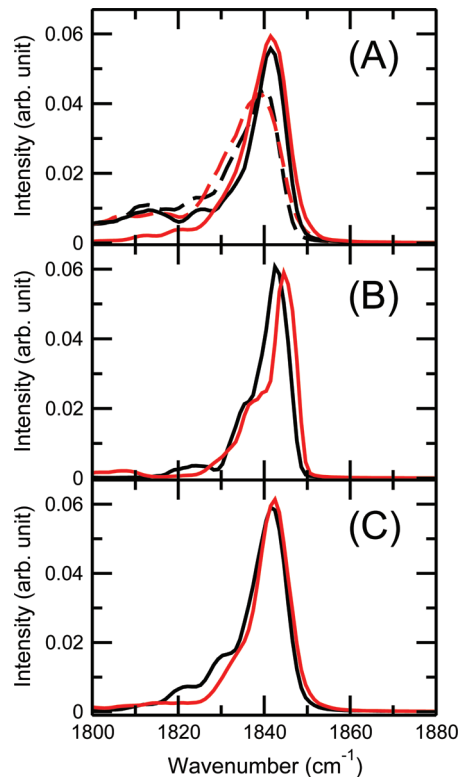


Figure 4. IR spectra of NO in Mb. Black curves correspond to B-state spectra, whereas red ones are for state C. (A) Spectra from 20 independent NPT simulations at 300 K for 1 ns with PBC. The dashed curves are pocket-unspecific spectra from simulations starting in states B and C. The solid curves are pocket-specific spectra. (B) IR spectra obtained from five independent NPT simulations at 100 K for 600 ps with PBC. (C) IR spectra computed from NVE simulations using SBC, with infinite electrostatic cutoff.

on the red side of the main peak, which is different from the pocket-specific spectrum (red solid line). This contribution comes from sampling the B-state accessed during the simulations, although the simulations have been started from the C-state.

Convergence tests for the spectra were carried out as follows. The IR spectra were computed from 500 ps and 1.0, 1.5, and 2.0 ns, respectively (see Figure 5), and averaged over all 20 independent trajectories starting from the B- or C-state. They are compared in two ways. In one of them, the spectra are scaled to identical peak maximum heights, whereas in the other (inset) they are scaled to identical total absorbance. In both representations, the peak positions are well converged already after 500 ps, whereas additional features become somewhat more pronounced for longer simulation times. The overall shape of the spectra remains unchanged after 2 ns, which suggests that such a simulation time together with the conformational averaging is appropriate for the purpose of the present work.

To obtain pocket-specific, conformationally averaged IR spectra at lower temperature, MD simulations (600 ps in length) were carried out at 100 K with the NO molecule in the B- and C-states initially. In the simulations at this temperature, the NO molecule did not move from one cavity to the other. The spectra, averaged over five independent runs (i.e., a total of 3 ns), are reported in Figure 4B. It is found that the peak positions in the different cavities show only small difference and

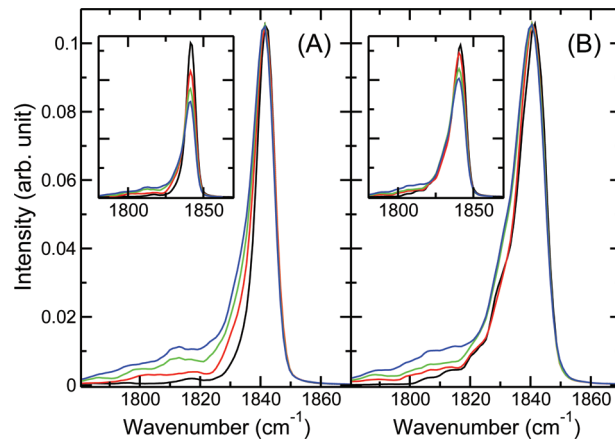


Figure 5. Time-dependent IR spectra at 300 K for the initial configuration of (A) B-state and (B) C-state. Averaged spectra from the first 0.5, 1.0, 1.5, and 2.0 ns from all simulations are shown in black, red, green, and blue, respectively. The spectra normalized with respect to the peak height are shown in full scale, and the spectra normalized with respect to the integrated area are shown in the insets for comparison.

that the FWHMs of the peaks are smaller for IR spectra at low temperature. A satellite band at the slightly lower frequency from the main peak can be discerned in the spectra at 100 K, which indicates that there are at least two different conformational substates for each of the states (B and C): 1843 and 1836 cm^{-1} for the B-state and 1845 and 1839 cm^{-1} for the C-state, respectively. This observation is in accord with IR spectra previously computed from MD simulations with a three-point fluctuating NO-charge model,²⁴ where the spectra of NO fell into a very narrow range between 1915 and 1922 cm^{-1} at various temperatures (50–300 K), in strong contrast with the spectra for CO in Mb.^{22,23,62,63}

For validating the treatment of the electrostatic interactions, IR spectra were also calculated from SBC simulations at 100 K without electrostatic cutoff (i.e., infinite cutoff). The peak positions and shapes from simulations without cutoff are quite similar to those from the simulations with cutoff, as shown in Figure 4C. The frequencies from the SBC simulations are at 1842 cm^{-1} for the B-state and 1843 cm^{-1} for the C-state, compared with 1843 and 1845 cm^{-1} from PBC simulations. This implies that the protein environment around NO is not affected much by the boundary conditions. From simulations at 100 K with modified LJ parameters for NO ($\Delta r_{\min} = \pm r_{\min}^{(0)}/10$), only insignificant changes in the IR spectra are found (spectra not shown).

Experimentally, the IR spectra of photodissociated NO in Mb under various conditions have been recently reported.²⁹ In wild-type Mb(II) at 4 K, the NO stretching frequencies are found at 1852 and 1857 cm^{-1} for the B-state and at 1865 and 1869 cm^{-1} for the C-state (with an error of $\pm 2 \text{ cm}^{-1}$) which corresponds to substate splittings of 5 and 4 cm^{-1} , respectively. This compares well with splittings of 7 cm^{-1} (B-state) and 6 cm^{-1} (C-state) at 100 K and 3 cm^{-1} (B-state) and 4 cm^{-1} (C-state) at 20 K from the present simulations. The split IR peaks most likely reflect distinguishable conformational substates of NO in the B- and C-states. At 20 K, the free energy computed from the probability distribution as a function of the Fe–N–O angle indeed finds two (B-state) and three (C-state) discrete substates, as shown in Figure 6. They are characterized by Fe–

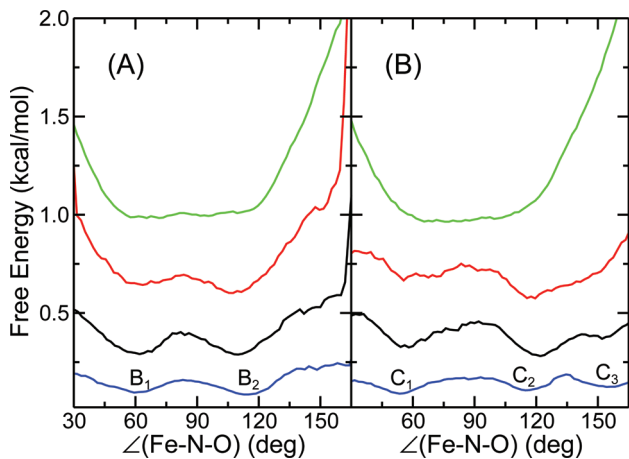


Figure 6. The free energy for NO as a function of the Fe–N–O angle in (A) the heme pocket and (B) the Xe₄ cavity at 300 K (green), 100 K (red), 50 K (black), and 20 K (blue).

N–O angles of 60 and 110° for the B-state and 60, 110, and 150° for the C-state.

The two NO-orientations in the B-state with Fe–N–O angles of 60 and 110°, respectively, are reported in Figure 7, where NO is shown in blue for 60° and in red for 110°. The free energy profile (FEP) computed from the probability distribution for temperatures between 20 and 300 K for both spectroscopic states is reported in Figure 6. At 20 K, the NO can sample the substates for sufficiently long periods of time. The discrete states are still found at 50 K, although the barriers between them are quite low (~0.16 kcal/mol), whereas at 100 K they start to slowly disappear. Due to rapid interconversion between the states, they are not discrete anymore at 300 K. The IR spectra corresponding to $T = 20$ K are shown in Figure 8. The peak positions are 1840 and 1843 cm⁻¹ for the B-state and 1839, 1842, and 1843 cm⁻¹ for the C-state. This demonstrates that the states are spectroscopically different and expected

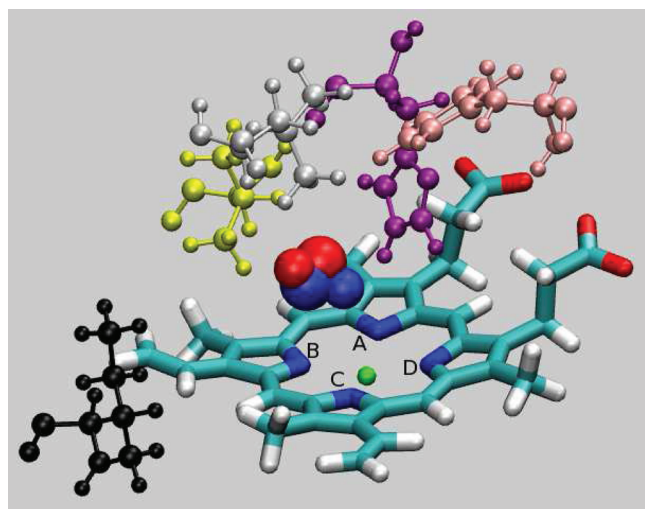


Figure 7. The NO molecule and residues lining the heme pocket for the B-state with Fe–N–O angles of 60 and 110°. NO is shown in blue spheres for 60° and in red spheres for 110°. The larger sphere corresponds to the N atom and the smaller one to the O atom of the NO molecule. The heme group is shown in licorice and amino acid residues in ball and stick with different colors: Leu29 (silver), Phe46 (pink), His64 (purple), Val68 (yellow), and Ile107 (black).

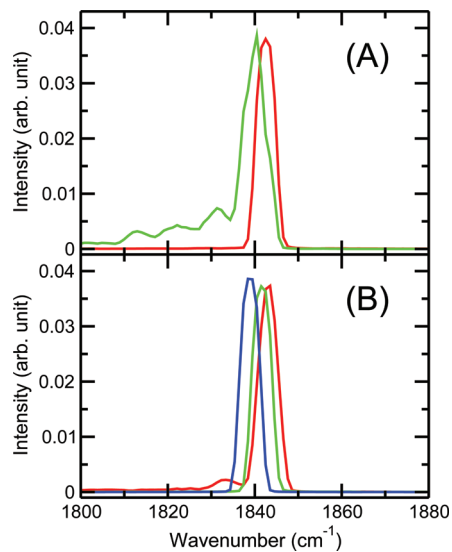


Figure 8. IR spectra of NO at 20 K for different conformational substates, characterized by the Fe–N–O angle in the B- or C-state. (A) B-state spectra with Fe–N–O angles of 60 and 110° in red and green, respectively, and (B) C-state spectra for angles 60, 110, and 150° in red, green, and blue, respectively.

splittings within one state are of the order of a few wavenumbers which agrees with experiments.²⁹

Following the discovery of additional substates for CO in Mb,^{64–66} the orientational preferences of NO in the B- and C-states were characterized in more detail. For this, the orientational probability functions (OPFs) of NO relative to the heme were computed from the simulations at 20 K. The coordinate θ is defined as the angle between the N–O bond vector and the surface normal to the heme plane and ϕ as that between the projection of the N–O bond vector onto the heme plane and the vector connecting nitrogen atoms N_A and N_C of the heme (see Figure 7). The surface normal is defined as the normal vector through the Fe-atom orthogonal to the average plane containing the four heme-nitrogen atoms. OPFs are reported in Figure 9 and show several characteristic maxima. For the B-state, they include B₁ and B₂ which correspond to the two minima in Figure 6. As the OPF shows, substate B₂ consists

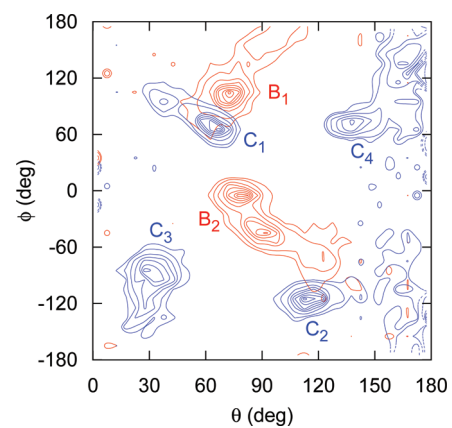


Figure 9. Orientational probability functions in the B- and C-states at 20 K shown in red and blue, respectively. The definitions of θ and ϕ are given in the text. The substates are labeled as B₁ and B₂ for B-state and C₁, C₂, C₃, and C₄ for C-state. These labels correspond to those shown in Figure 6.

of two nearby maxima which merge when averaged over the Fe–N–O angle. For conformational substate C, four favorable positions C_1 through C_4 are found. Inspection of Figure 6 shows that state C_4 is masked when the FEPs are considered as a function of the Fe–N–O angle.

IR spectra from simulations with a previously developed three-point charge model of NO²⁴ at 20 K show somewhat wider variations in the peak positions compared with those obtained here. In the B-state, frequencies range from 1836 to 1851 cm⁻¹ and in the C-state from 1834 to 1854 cm⁻¹. However, in both cases (three-point charge and MTP models of NO), the difference in the peak positions of NO in the heme pocket or Xe4 cavity is small. Finally, four independent simulations of 300 ps at 20 K were carried out with a conventional two-point static charge model with $Q_{00} = 0.065e$ for N and $-0.065e$ for O. It is found that the average peak maximum of the computed IR absorption is at 1840 and 1841 cm⁻¹ in the B- and C-states, respectively. The splitting of the peaks is about 6 cm⁻¹ for each state at 20 K. The IR spectra computed from 300 ps trajectories at 300 K with the two-point static charge model show a single peak, whereas simulations with the MTP model find a broader shoulder on the red side (see Figure 4A). Thus, for spectroscopic applications, the multipolar model is clearly superior in capturing details such as band splittings. This is consistent with previous work on CO in Mb.^{21–23,67}

In the experiments, the two bands for the B- and C-states are red-shifted by 7 and 24 cm⁻¹ compared to the gas-phase spectrum.²⁹ This is not reproduced by the MD simulations, which find a blue shift of 6–7 cm⁻¹ with the MTP model. As already discussed above, this difference is *not* related to convergence of the simulations (see Figure 5). In order to better understand this observation, computationally much more demanding QM/MM//MD simulations were carried out. One possibility is that the protein environment perturbs the NO-electron distribution sufficiently strongly, which could lead to changes in the bond order and therefore alter the vibrational frequency. We performed four independent QM/MM//MD simulations at 20 K for 100 ps using CHARMM interfaced with GAMESS,⁶⁸ where NO was treated with QM (ROHF/6-31G) and all other atoms with MM. The IR frequencies of NO computed from the dipole moment autocorrelation function were then compared with that of free NO at the same level of theory. The average peak maximum occurs at 2133 cm⁻¹ for NO in both the B- and C-states, compared with 2125 cm⁻¹ for free NO. As for the force field simulations above, blue shifts are found. A similar comparison was made for simulations performed with SCC-DFTB⁶⁹ instead of ROHF/6-31G using CHARMM, which gave 2134 cm⁻¹ for the B- and C-states on average, compared with 2130 cm⁻¹ for free NO. Again, the absorption peak is shifted to the blue for the NO molecule in the protein compared to the gas phase. In summary, from all simulations carried out so far (DMA with fluctuating point charges, QM(ROHF/6-31G)/MM, and QM(SCC-DFTB)/MM), one concludes that the NO-stretching frequency is particularly sensitive to its electrostatic environment. Thus, it is possible that improvements in the heme and protein force field would be required to capture the experimentally observed red shift.

To corroborate this, optimizations and frequency calculations for a heme-His93 model system with unbound NO in the gas phase were carried out at the B3LYP/6-31G(d,p) level of theory. For free gas-phase NO, the frequency is 1992 cm⁻¹,

compared to 1972 cm⁻¹ with NO above the heme. In this calculation, the heme was constrained to a planar geometry and all other coordinates were fully relaxed. If the heme is allowed to bend, the NO stretching frequency shifts to 1943 cm⁻¹. Thus, in both cases (planar and bent heme), a red shift between 20 and 49 cm⁻¹ is found for the gas-phase system. Although the magnitude is overestimated—probably due to anharmonicity and environmental effects of the protein—these calculations find a red shift and confirm that if the heme moiety is treated at the same level of electronic structure theory as the NO ligand, red shifts in the NO stretch frequency are expected, which agrees with experiment.²⁹

To conclude, we find that, while shifts *within* one given conformational substate (B or C) can be reliably captured with improved electrostatic models based on fluctuating MTPs, shifts *between* the two substates and the overall red shift of the bands compared to gas-phase NO cannot be quantitatively described. On the basis of the above calculations, we expect that improvements in the heme and protein force field parametrization are required for this. Indeed, it was recently found that the heme force field could be improved in several ways, including the charge distribution.^{70,71}

Free Energy for Migration. To estimate the relative free energies for NO in the heme pocket and the Xe4 cavity, and the barrier between them, umbrella sampling was used.⁷² As reported previously, a suitable reaction coordinate δ for this transition is the distance between the center of mass of NO and the Fe atom of the heme group.^{24,58} The FEP is shown in Figure 10. Analysis of the data with WHAM⁵⁷ yields a free energy difference between B- and C-states of $\Delta G_{B/C} = 1.3$ kcal/mol with a forward barrier of $\Delta G_{B \rightarrow C}^{\ddagger} = 2.0$ kcal/mol and a reverse barrier of $\Delta G_{B \leftarrow C}^{\ddagger} = 0.7$ kcal/mol. Errors in the FEPs were estimated from analyzing fractions of the available data (100 ps) per window, namely, 50, 60, and 75 ps. This leads to a differential stabilization energy of $\Delta G_{B/C} = 1.1 \pm 0.2$ kcal/mol and barriers of $\Delta G_{B \rightarrow C}^{\ddagger} = 1.8 \pm 0.2$ kcal/mol and $\Delta G_{B \leftarrow C}^{\ddagger} = 0.7 \pm 0.1$ kcal/mol. In agreement with the unbiased simulations (see below), it is found that NO is stabilized in the B-state

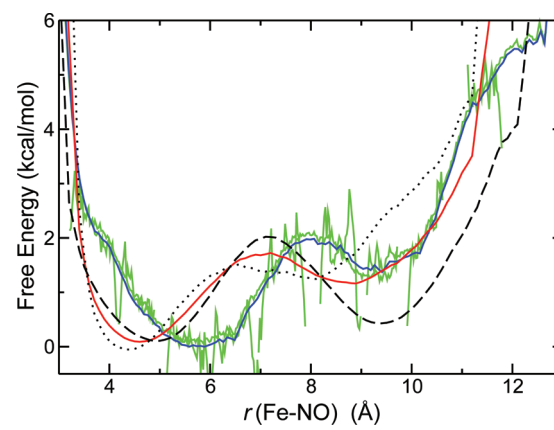


Figure 10. Free energy profiles for NO migration between the B- and C-states in Mb as a function of the distance between the center of mass of NO and the heme-Fe atom. The blue trace corresponds to results from umbrella sampling (data accumulation of 100 ps) analyzed with WHAM, the green trace to that analyzed without WHAM, and the red trace to the analysis of the 40 unbiased MD trajectories of 2 ns each. The red curve is the average over the FEPs obtained from analyzing the individual 20 simulations initiated from the B- (dotted black) and the C-states (dashed black).

relative to the C-state. An alternative way to analyze the data is to match the data individually for each umbrella window (see Computational Methods). The FEP obtained this way is shown in green in Figure 10 and yields similar barriers as the WHAM analysis. In addition to the umbrella sampling simulations of 100 ps with $K = 5.0 \text{ kcal}\cdot\text{mol}^{-1}\cdot\text{\AA}^{-2}$, we also performed 50 ps simulations with $K = 2.5 \text{ kcal}\cdot\text{mol}^{-1}\cdot\text{\AA}^{-2}$ and 100 ps simulations with $K = 10.0 \text{ kcal}\cdot\text{mol}^{-1}\cdot\text{\AA}^{-2}$ to assess their effect on the FEPs. The simulations (results not shown) with different K values gave similar results as those reported in Figure 10.

As umbrella sampling introduces a bias and 2 ns-unbiased simulations readily sample the B- to C-transition, the 40 independent trajectories (20 initiated from the B- and C-states, respectively) at 300 K were analyzed and FEPs were derived from both sets. A total of ~ 100 transitions for $B \rightleftharpoons C$ were observed. Because individual transitions can be immediately followed by a reverse transition, only those which were separated by more than 10 ps were counted. The data was analyzed by computing the probability distribution $P(\delta)$ and then using $G(\delta) = -k_B T \ln[P(\delta)] + C$, where $G(\delta)$ is the free energy at δ , C is a constant, T is the temperature, and k_B is the Boltzmann constant. This yields a differential stabilization free energy of $\Delta G_{B/C}^\ddagger = 1.0 \text{ kcal/mol}$, a forward barrier of $\Delta G_{B \leftarrow C}^\ddagger = 1.7 \text{ kcal/mol}$, and a reverse barrier of $\Delta G_{B \leftarrow C}^\ddagger = 0.7 \text{ kcal/mol}$, all of which are within the error bars of the umbrella sampling simulations. Slight differences in the stabilization and barrier energies and the position of the minimum energy between umbrella sampling and unbiased estimate may either be related to the bias imposed by the umbrella sampling or due to local relaxation.⁷³ Increasing the total simulation time beyond 80 ns may also slightly change the free energy profile. However, the agreement between the two approaches is reassuring. With CO, it was found that the ligand typically prefers localization in state C over state B.^{58,74,75} Depending on the simulation details, the differential stabilization $\Delta G_{B/C}^\ddagger$ ranges from 1 to 3.5 kcal/mol in favor of the spectroscopic C-state (Xe4 pocket) which is opposite to NO.

Experimentally, the NO rebinding kinetics to Mb has been investigated using IR¹⁰ and electronic⁷ spectroscopies. The optical measurements have also considered the temperature dependence of this process in more detail. In particular, the ultrafast experiments identified a rapid (~ 10 ps) and a slower (~ 200 ps) phase which were associated with the rebinding ($B \rightarrow A$) and a migration ($X \rightarrow B$) step from an a priori unknown site X.⁷ Analysis yields a $X \rightarrow B$ barrier of 3 kJ/mol (i.e., ~ 0.7 kcal/mol). Such a barrier is in very favorable agreement with the present simulations $\Delta G_{B \leftarrow C}^\ddagger = 0.7 \text{ kcal/mol}$ for the C to B transition. Conversely, previous implicit ligand sampling simulations found $\Delta G_{B \leftarrow C}^\ddagger \approx 4 \text{ kcal/mol}$ for this transition and therefore considerably overestimate the stabilization of NO in the Xe4 pocket compared to both experiment and the present simulations.⁶⁵ It was already suggested from the experiments that state X corresponds to the spectroscopic C-state (structural Xe4 pocket) which is supported by the present simulations.

IV. CONCLUSIONS

The use of distributed multipoles (MTPs) has been extended to open-shell systems. This generalized model was applied to the dynamics, spectroscopy, and migration energetics of photodissociated NO in Mb around the active sites. For the spectroscopic observables, it was found that within one conformational substate (B or C) the splitting of the spectrum

can be correctly described compared with recent experiments. This is in line with related simulations for photodissociated CO in Mb. The existence of additional substates for NO, separated by low barriers (below 1 kcal/mol), for the spectroscopic B- and C-states also agrees with experiments and simulations on unbound CO in Mb.^{65,66} The relative frequency shifts between the two states, which was never investigated before, and red shifts for the NO frequencies in Mb compared to gas-phase NO could not be reproduced. Because (a) two different flavors of QM/MM//MD simulations (where only the NO is treated quantum mechanically) also fail to capture such effects and (b) gas-phase ab initio calculations on a fairly large heme-model system do find a red shift, it is likely that improved electrostatics for the surrounding heme and protein residues is required. This is in line with previous work on the energetics and spectroscopy of bound MbCO which suggested that there is potential for improvement for the heme group.^{70,71,76} Compared to experiment,⁷ the ligand migration barrier between the spectroscopic B- and C-states is remarkably well captured. These findings confirm that nitric oxide experiences lower migration barriers than CO.^{9,10,14,15} Finally, the simulations allow “state X” from the experiments to be assigned to the Xe4 pocket.⁷

AUTHOR INFORMATION

Notes

The authors declare no competing financial interest.

ACKNOWLEDGMENTS

The authors gratefully acknowledge financial support from the Swiss National Science Foundation through grant 200021-117810 and NCCR MUST.

REFERENCES

- (1) Frauenfelder, H.; McMahon, B. H.; Austin, R. H.; Chu, K.; Groves, J. T. *Proc. Natl. Acad. Sci. U.S.A.* **2001**, *98*, 2370–2374.
- (2) Coyle, C. M.; Vogel, K. M.; Rush, T. S. III; Kozlowski, P. M.; Williams, R.; Spiro, T. G.; Dou, Y.; Ikeda-Saito, M.; Olson, J. S.; Zgierski, M. Z. *Biochemistry* **2003**, *42*, 4896–4903.
- (3) Cornelius, P.; Hochstrasser, R.; Steele, A. *J. Mol. Biol.* **1983**, *163*, 119–128.
- (4) Petrich, J. W.; Lambry, J. C.; Kuczera, K.; Karplus, M.; Poyart, C.; Martin, J. L. *Biochemistry* **1991**, *30*, 3975–3987.
- (5) Gibson, Q.; Regan, R.; Elber, R.; Olson, J.; Carver, T. *J. Biol. Chem.* **1992**, *267*, 22022–22034.
- (6) Ikeda-Saito, M.; Dou, Y.; Yonetani, T.; Olson, J.; Li, T.; Regan, R.; Gibson, Q. *J. Biol. Chem.* **1993**, *268*, 6855–6857.
- (7) Ionascu, D.; Gruia, F.; Ye, X.; Yu, A.; Rosca, F.; Demidov, C. B. A.; Olson, J. S.; Champion, P. M. *J. Am. Chem. Soc.* **2005**, *127*, 16921–16934.
- (8) Kruglik, S. G.; Yoo, B.-K.; Franzen, S.; Vos, M. H.; Martin, J.-L.; Negrerie, M. *Proc. Natl. Acad. Sci. U.S.A.* **2010**, *107*, 13678–13683.
- (9) Kim, S.; Jin, G.; Lim, M. *J. Phys. Chem. B* **2004**, *108*, 20366–20375.
- (10) Kim, S.; Lim, M. *J. Am. Chem. Soc.* **2005**, *127*, 8908–8909.
- (11) Li, H.; Elber, R.; Straub, J. E. *J. Biol. Chem.* **1993**, *268*, 17908–17916.
- (12) Schaad, O.; Zhou, H.-X.; Szabo, A.; Eaton, W. A.; Henry, E. R. *Proc. Natl. Acad. Sci. U.S.A.* **1993**, *90*, 9547.
- (13) Meuwly, M.; Becker, O. M.; Stote, R.; Karplus, M. *Biophys. Chem.* **2002**, *98*, 183–207.
- (14) Nutt, D. R.; Meuwly, M. *Biophys. J.* **2006**, *90*, 1191–1201.
- (15) Danielsson, J.; Meuwly, M. *J. Chem. Theory Comput.* **2008**, *4*, 1083–1093.
- (16) Franzen, S. *Proc. Natl. Acad. Sci. U.S.A.* **2002**, *99*, 16754–16759.

- (17) Tilton, R. F. Jr.; Kuntz, I. D. Jr.; Petsko, G. A. *Biochemistry* **1984**, *23*, 2849–2857.
- (18) Schotte, F.; Lim, M.; Jackson, T. A.; Smirnov, A. V.; Soman, J.; Olson, J. S.; Phillips, G. N.; Wulff, M.; Anfinrud, P. A. *Science* **2003**, *300*, 1944–1947.
- (19) Beece, D.; Eisenstein, L.; Frauenfelder, H.; Good, D.; Marden, M. C.; Reinisch, L.; Reynolds, A. H.; Sorensen, L. B.; Yue, K. T. *Biochemistry* **1980**, *19*, 5147–5157.
- (20) Lamb, D. C.; Nienhaus, K.; Arcovito, A.; Draghi, F.; Miele, A. E.; Brunori, M.; Nienhaus, G. U. *J. Biol. Chem.* **2002**, *277*, 11636–11644.
- (21) Plattner, N.; Meuwly, M. *Biophys. J.* **2008**, *94*, 2505–2515.
- (22) Nutt, D. R.; Meuwly, M. *Biophys. J.* **2003**, *85*, 3612–3623.
- (23) Nutt, D. R.; Meuwly, M. *Proc. Natl. Acad. Sci. U.S.A.* **2004**, *101*, 5998–6002.
- (24) Nutt, D. R.; Meuwly, M. *ChemPhysChem* **2004**, *5*, 1710–1718.
- (25) Nutt, D. R.; Meuwly, M. *ChemPhysChem* **2007**, *8*, 527–536.
- (26) Mishra, S.; Meuwly, M. *Biophys. J.* **2009**, *96*, 2105–2118.
- (27) Lutz, S.; Nienhaus, K.; Nienhaus, G. U.; Meuwly, M. *J. Phys. Chem. B* **2009**, *113*, 15334–15343.
- (28) Nienhaus, K.; Lutz, S.; Meuwly, M.; Nienhaus, G. U. *ChemPhysChem* **2010**, *11*, 119–129.
- (29) Nienhaus, K.; Palladino, P.; Nienhaus, G. U. *Biochemistry* **2008**, *47*, 935–948.
- (30) Brooks, B. R.; et al. *J. Comput. Chem.* **2009**, *30*, 1545–1614.
- (31) Brucker, E. A.; Olson, J. S.; Ikeda-Saito, M.; Phillips, G. N. Jr. *Proteins* **1998**, *30*, 352–356.
- (32) Protein Data Bank, <http://www.rcsb.org>.
- (33) Merchant, K. A.; Noid, W. G.; Thompson, D. E.; Akiyama, R.; Loring, R. F.; Fayer, M. D. *J. Phys. Chem. B* **2003**, *107*, 4–7.
- (34) Meuwly, M. *ChemPhysChem* **2006**, *7*, 2061–2063.
- (35) Nienhaus, K.; Olson, J. S.; Franzen, S.; Nienhaus, G. U. *J. Am. Chem. Soc.* **2005**, *127*, 40–41.
- (36) Jorgensen, W. L.; Chandrasekhar, J.; Madura, J. D.; Impey, R. W.; Klein, M. L. *J. Chem. Phys.* **1983**, *79*, 926–935.
- (37) Ryckaert, J.-P.; Ciccotti, G.; Berendsen, H. J. C. *J. Comput. Phys.* **1977**, *23*, 327–341.
- (38) Yoneya, M.; Berendsen, H. J. C.; Hirasawa, K. *Mol. Simul.* **1994**, *13*, 395–405.
- (39) Brooks, C. L. III; Brünger, A.; Karplus, M. *Biopolymers* **1985**, *24*, 843–865.
- (40) Tsuji, K.; Imaizumi, M.; Oyoshi, A.; Mochida, I.; Fujitsu, H.; Takeshita, K. *Inorg. Chem.* **1982**, *21*, 721–725.
- (41) Toma, H. E.; Alexiou, A. D. P.; Dovidauskas, S. *Eur. J. Inorg. Chem.* **2002**, *2002*, 3010–3017.
- (42) Berens, P.; K., W. *J. Chem. Phys.* **1981**, *74*, 4872–4882.
- (43) Frisch, M. J.; Trucks, G. W.; Schlegel, H. B.; Scuseria, G. E.; Robb, M. A.; Cheeseman, J. R.; Montgomery, J. A. Jr.; Vreven, T.; Kudin, K. N.; et al. *Gaussian 03*, revision C.01; Gaussian, Inc.: Wallingford, CT, 2004.
- (44) Stone, A. J. *J. Chem. Theory Comput.* **2005**, *1*, 1128–1132.
- (45) Nelson, R. D. Jr.; Lide, D. R. Jr.; Maryott, A. A. *Selected values of electric dipole moments for molecules in the gas phase*; National Bureau of Standards, United States Department of Commerce Technical Report NSRDS-NBS10, 1967.
- (46) Hill, R. M.; Smith, W. V. *Phys. Rev.* **1951**, *82*, 451.
- (47) Stone, A. J. *The Theory of Intermolecular Forces*; Oxford University Press: Oxford, U.K., 1996.
- (48) Plattner, N.; Meuwly, M. *J. Mol. Model.* **2009**, *15*, 687–94.
- (49) Lee, M. W.; Meuwly, M. *J. Phys. Chem. A* **2011**, *115*, 5053–5061.
- (50) Allen, M. P.; Tildesley, D. J. *Computer Simulation of Liquids*; Oxford University Press: New York, 1987.
- (51) Meller, J.; Elber, R. *Biophys. J.* **1998**, *74*, 789–802.
- (52) Ma, J.; Huo, S.; Straub, J. *J. Am. Chem. Soc.* **1997**, *119*, 2541–2551.
- (53) Auer, B. M.; Kumar, R.; Schmidt, J. R.; Skinner, J. L. *Proc. Natl. Acad. Sci. U.S.A.* **2007**, *104*, 14215–14220.
- (54) Auer, B. M.; Skinner, J. L. *J. Chem. Phys.* **2008**, *128*, 224511.
- (55) Torrie, G. M.; Valleau, J. P. *J. Comput. Phys.* **1977**, *23*, 187–199.
- (56) Kumar, S.; Rosenberg, J. M.; Bouzida, D.; Swendsen, R. H.; Kollman, P. A. *J. Comput. Chem.* **1992**, *13*, 1011–1021.
- (57) Kumar, S.; Rosenberg, J. M.; Bouzida, D.; Swendsen, R. H.; Kollman, P. A. *J. Comput. Chem.* **1995**, *16*, 1339–1350.
- (58) Banushkina, P.; Meuwly, M. *J. Phys. Chem. B* **2005**, *109*, 16911–16917.
- (59) Silvi, B.; Savin, A. *Nature* **1994**, *371*, 683–686.
- (60) Bossa, C.; Anselmi, M.; Roccatano, D.; Amadei, A.; Vallone, B.; Brunori, M.; Di Nola, A. *Biophys. J.* **2004**, *86*, 3855–3862.
- (61) Bossa, C.; Amadei, A.; Daidone, I.; Anselmi, M.; Brunori, B. V. M.; Di Nola, A. *Biophys. J.* **2005**, *89*, 465–474.
- (62) Lim, M.; Jackson, T. A.; Anfinrud, P. A. *J. Am. Chem. Soc.* **2004**, *126*, 7946–7957.
- (63) Nienhaus, K.; Deng, P.; Krieg, J. M.; Nienhaus, G. U. *Biochemistry* **2003**, *42*, 9633–9646.
- (64) Cohen, J.; Arkhipov, A.; Braun, R.; Schulter, K. *Biophys. J.* **2006**, *91*, 1844–1857.
- (65) Banushkina, P.; Meuwly, M. *J. Chem. Phys.* **2007**, *127*, 135101.
- (66) Krieg, J. M.; Nienhaus, K.; Deng, P.; Fuchs, J.; Nienhaus, G. U. *Proc. Natl. Acad. Sci. U.S.A.* **2003**, *100*, 7069–7074.
- (67) Devereux, M.; Plattner, N.; Meuwly, M. *J. Phys. Chem. A* **2009**, *113*, 13199–13209.
- (68) Schmidt, M. W.; Baldridge, K. K.; Boatz, J. A.; Elbert, S. T.; Gordon, M. S.; Jensen, J. H.; Koseki, S.; Matsunaga, N.; Nguyen, K. A.; Su, S. J.; Windus, T. L.; Dupuis, M.; Montgomery, J. A. *J. Comput. Chem.* **1993**, *14*, 1347–1363.
- (69) Elstner, M.; Porezag, D.; Jungnickel, G.; Elsner, J.; Haugk, M.; Frauenheim, T.; Suhai, S.; Seifert, G. *Phys. Rev. B* **1998**, *58*, 7260–7268.
- (70) Autenrieth, F.; Tajkhorshid, E.; Baudry, J.; Luthey-Schulten, Z. *J. Comput. Chem.* **2004**, *25*, 1613–1622.
- (71) Devereux, M.; Meuwly, M. *J. Chem. Inf. Model.* **2010**, *50*, 349–357.
- (72) Kottalam, J.; Case, D. A. *J. Am. Chem. Soc.* **1988**, *110*, 7690–7697.
- (73) Banushkina, P.; Meuwly, M. *J. Chem. Theory Comput.* **2005**, *1*, 208–214.
- (74) Ceccarelli, M.; Anedda, R.; Casu, M.; Ruggerone, P. *Proteins* **2008**, *71*, 1231–1236.
- (75) Plattner, N.; Meuwly, M. *Biophys. J.* **2012**, *102*, 333–341.
- (76) Devereux, M.; Meuwly, M. *Biophys. J.* **2009**, *96*, 4363–4375.